Accuracy of complex internal channels produced by laser powder bed fusion process

Accuracy of complex internal channels produced by laser powder bed fusion process

Flaviana Calignano [a,*], Oscar Antonio Peverini [b], Giuseppe Addamo [b], Luca Iuliano [a]

[a] *Department of Management and Production Engineering, Politecnico di Torino, Corso Duca degli Abruzzi, 24, Turin, Italy; flaviana.calignano@polito.it, luca.iuliano@polito.it*

[b] *Istituto di Elettronica e di Ingegneria dell'Informazione e delle Telecomunicazioni, National Research Council of Italy (CNR-IEIIT), Corso Duca degli Abruzzi 24, Turin, Italy; oscar.peverini@ieiit.cnr.it, giuseppe.addamo@ieiit.cnr.it*

Abstract

Additive manufacturing (AM) technology has great potential in manufacturing complex internal channels for several applications such as satellite-communication microwave systems. These systems can have complex shapes and make traditional finishing processes a challenge for additive parts. Therefore, it is desirable that the internal surfaces are as close as possible to the tolerance of the field of application. In this study, a complex component, a unique waveguide device with bending, twisting and filtering functionalities, has been designed and manufactured in AlSi10Mg alloy through laser powder bed fusion (L-PBF) process. Three different prototypes with three different curvature (*R* of 50 mm, 40 mm and 30 mm), operating in Ku/K band, have been manufactured and tested showing a very good agreement with the desired performances. Using 3D scan data, the internal deviations from the CAD model have been evaluated showing an average deviation of the internal areas of about 0.08 mm, 0.046 mm and 0.023 mm from the CAD model for the *R* of 50 mm, 40 mm and 30 mm respectively The surface roughness measured in the internal channel is about R_a (arithmetic average roughness) of 8 μm ± 1.3 μm and R_z (average maximum height of the roughness profile) of 62.3 μm ± 0.34 μm.

Keywords: Additive Manufacturing; laser powder bed fusion; integration waveguide subsystem.

1. Introduction

Antenna-feed chains are microwave systems widely used for several Space-born applications, including satellite communication, Earth observation and radio-astronomy. In this context, there is an increasing interest in allocating several channels in the same chain with subsequent advantages in term of mass and cost reduction. As a drawback, the relevant electromagnetic architectures become more and more complex, so that their realization is often not feasible or too expensive exploiting conventional manufacturing processes. This problem is even more evident in the case of arrays of feeds and/or systems where high-power handling capability is required. A possible solution can be represented by additive manufacturing (AM) technologies thanks to their potential in manufacturing almost free-form devices and in functionality integration [1]. If classical machining technologies are employed, the waveguide circuitry turns into a certain number of discrete components separately manufactured with subsequent increment of mass, volume and assembling complexity. To overcome these problems, in the last ten years, there has been an increasing interest in AM technologies from the microwave community. The realized devices span from waveguide components to antennas operating in the X-W band range (8-110 GHz) (Figure 1) [2–7].

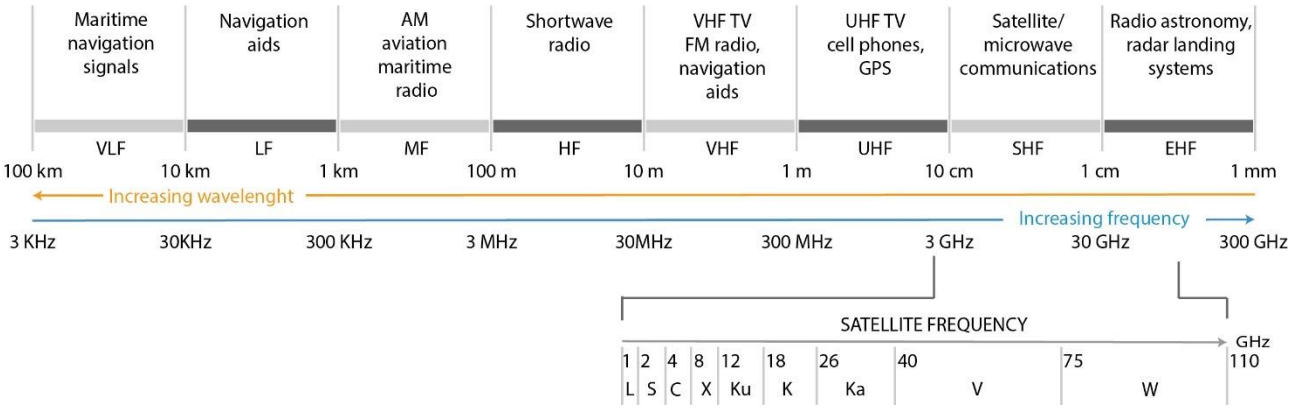

Figure 1. Frequency spectrum with definition of satellite frequency bands.

Among the various AM techniques, laser-based powder bed fusion of metal (L-PBF) exhibits the capability of manufacturing vey compact and complex payloads for Space-borne applications [7,8]. In this process, layers of metal powders are fused layer upon layer by a high-power laser. Each layer is created by fusing the layer of powder relative to the areas of the cross-section of the 3D CAD (computer aided design) which consolidates and merges with the underlying layer. This technology offers several advantages for radio frequency (RF) engineers, such as near-net shape manufacturing, reduced tooling and fixtures, implementation of several functionalities (*i.e.*, electrical, structural or thermal) in a single component, thus reducing size, mass and costs. However, the L-PBF printed parts generally suffer from high surface roughness when compared with conventional machined parts: the value of the average roughness, R_a, of these surfaces is around 10 µm to 20 µm. Specific conditions of the melting pool can cause a defect in the molten material called 'balling'. This effect can break the edge of the melt pool, changing the shape of the layer. In addition, gravity inflects the melting wall for those layers that don't have a support, so that they can collapse into the underlying melted powder. The result is a much rougher surface on the lower surface of the component (called 'down-skin') than on the upper surfaces (called 'up-skin'). This difference between two surfaces is aggravated by the different heat dissipation between the areas in contact with the powder and those built on the solid material, thus creating thermal gradients. This, in turns, destabilizes the melt pool, thus interrupting the shape of the edge of the layer [9]. When the melting pool solidifies, the powder particles not completely melted adhere to the layer edge contributing to the final surface roughness. Surface roughness is a problem especially for complex internal surfaces of additively manufactured parts, because conventional machining and standard surface-finishing procedures are not able to reach the internal surfaces in complex monolithic parts. Because of warping and distortions that can happen on unsupported and overhanging areas [10,11], and depending on the orientation of construction, the down-facing surfaces of internal channels can exhibit both high roughness and low accuracy compared to middle sections. This can be a major problem in complex geometries with unreachable down-facing areas, because dimensional errors can be larger than the required tolerances and can lead to build failure. When the quantity of overhanging surface exceeds a threshold value, L-PBF requires the use of additional structures to support the weight of protruding geometries, to attach the component to the platform, and to ease heat dissipation [10]. However, these structures cannot be inserted inside complex channels of monolithic parts, because it would be impossible to remove them. By using 3D scan data, this study investigates the internal surfaces in terms of surface roughness and geometric deviations from the CAD model of a complex RF component. The latter has been designed

with the aim of integrating three electromagnetic features (namely filtering, bending and twisting) into a single mechanical part [12]. Three prototypes with different bending/twisting radii (R = 50 mm, 40 mm, and 30 mm) have been manufactured in AlSi10Mg alloy through L-PBF. First, the components have been tested at an electromagnetic level, and the results, already published in a previous study [12], are summarized in Section 4. Then, the prototypes have been cut in order to analyze the internal structure of the channels and to correlate the electromagnetics performances with the surface characteristics.

2. Experimental methodology

2.1 Benchmark for the capability of the L-PBF process

The Ku/K-band WR51-waveguide system shown in Figure 2(a) has been selected as a relevant benchmark in order to assess the capability of the L-PBF process to reduce the mass and to miniaturize dual-band dual-polarization waveguide antenna-feed chains [12]. The standard architecture of the WR51-waveguide system shown in Figure 2(a) consists of a 50-mm long bend, a twist with a length of 80 mm, and a straight 47-mm long section implementing the pass-band filter. These dimensions are needed in order to guarantee the typical electromagnetics requirements set by satellite telecommunications.

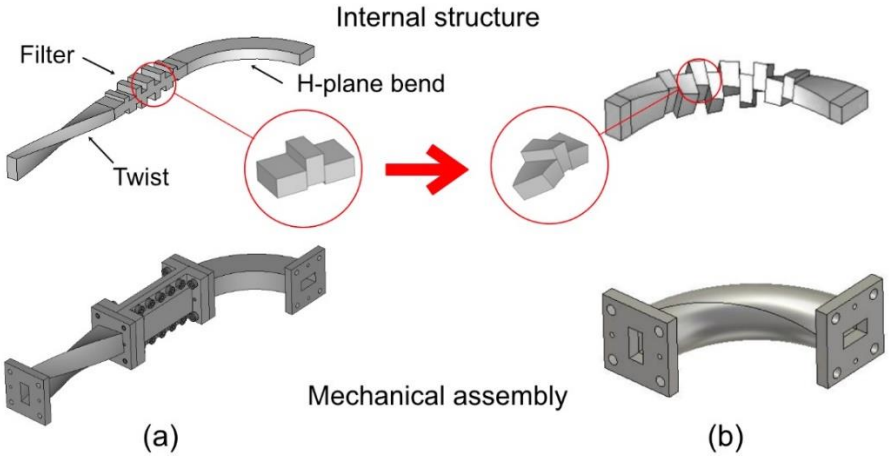

Figure 2. (a) Traditional WR51 waveguide subsystem; (b) redesigned WR51 waveguide component integrated.

The architecture of the integrated component is shown in Figure 2(b), and it cannot be easily produced in a single part through conventional processes (turning, milling, or electric discharge machining). Indeed, the design of this component has been carried out by exploiting the free-form capability of additive technology. Specifically, the L-PBF process has been considered, because it allows the development of metal components already assembled with high density (> 99.5%), good tensile strength and hardness [13–16], and a much lower surface roughness than that obtainable by another PBF process, namely the electron beam melting (EBM) [17–20]. With the aim of investigating the miniaturization capabilities offered by the L-PBF process, the integrated component of Figure 2(a) has been designed for three different values of the bending/twisting radius, that is R equal to 50 mm, 40 mm and 30 mm (Figure 3). It has to be pointed out that R = 30 mm is the minimum length sufficient to allocate the filter, *i.e.* the bend and twist are fully merged in the filter without any additional mass

or envelope. The three components have been electromagnetically designed and simulated by combining the method described in Peverini et al. [21] and CST Microwave Studio.

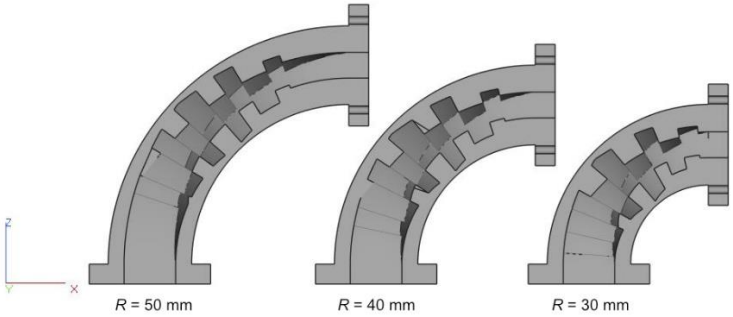

Figure 3. The integrated WR51 waveguide component in the three configurations.

The CAD model has been converted into a STL file in which the deviation control and the angle control [22] have been chosen, so as to reduce the approximation error and to make the discrepancies negligible between the electromagnetics responses of the two models. In particular, the values of 0.0015 mm and 10 degree have been used for the deviation and angle controls, respectively. The internal edges of the channel are rounded by 0.1 mm to avoid geometric errors due to the size of the laser diameter based on the process parameters used (Table 1). The orientation of the component on the platform is chosen as to make the surfaces of the internal channel self-supporting. Indeed, components have to be rotated around the three axes (x, y and z) in order to arrange the downward-facing surfaces of the internal channels with angles greater than 30°. In a previous study [10, 22], it has been found that it is possible to build self-supported structures in aluminum alloy for angles greater than this value. The supports, therefore, have been inserted only externally to anchor the prototypes to the building platform.

2.2 Equipment

An EOSINT M270 Dual-mode system has been used to build the AlSi10Mg components. This machine is equipped with an 200W Yb-fiber laser. During the manufacturing process, the building chamber is filled with an inert gas (argon) in order to keep the oxygen content less than 0.10 %. The L-PBF process parameters used are shown in Table 1. The scanning direction is rotated by 67° with respect to the previous layer. Correct optimization of process parameters, such as scanning options and beam offset, allows for a dimensional accuracy within 0.04 and 0.07 mm. For AlSi10Mg alloy, an equivalent surface electrical resistivity of approx. 10-20 μΩ are feasible [7]. The component was cut in two halves to investigate the accuracy of the surfaces between the different zones. Due to the geometrical conformation of the internal channel, during the construction each internal part has, at the same time, an area corresponding to the up-skin and an area corresponding to the down-skin. The two parts of each prototype have been digitized using an optical 3D scanner, Atos Compact Scan 2M by GOM GmbH that has an accuracy of about 0.001 mm. The measurements have been carried out according to the VDI/VDE 2634 – Part 3 and by using the GOM Inspect software for the inspection. Additionally, some internal surfaces have been detected using a Leica S9i stereomicroscope. The surface roughness of the internal channels has been measured using the RTP80 roughness tester by SM Metrology Systems. The values of roughness average (R_a) and average maximum height of the

profile (R_z) have been derived using a cut-off filter of 0.8 mm. Five measurements have been taken on each surface and the arithmetic mean of the measurements has been used

Process parameters	*Down-skin (3 layers)*	*Core*	*Up-skin (2 layers)*	*Contour*
Laser power [W]	190	195	190	80
Scan speed [mm/s]	900	800	800	900
Hatching distance [mm]	0.10	0.17	0.10	-
Layer thickness [μm]	30	30	30	-
Beam-spot size [μm]	100	100	100	100

Table 1. Process parameters used.

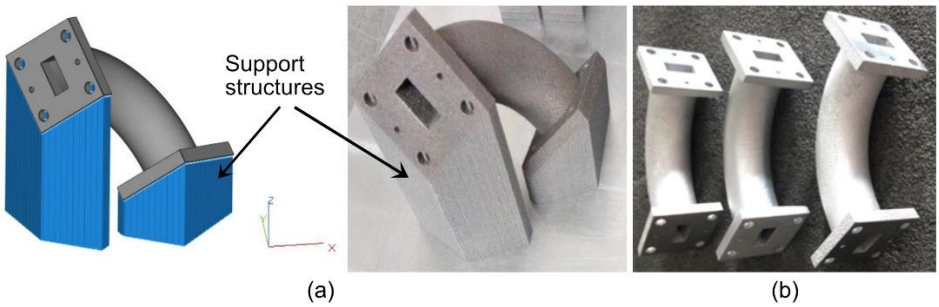

Figure 4. Integrated component: (a) building orientation and support structures; (b) prototypes after shoot peening for *R* of 30 mm (left), 40 mm (center) and 50 mm (right), respectively.

3. Results and discussion

Figure 4(a) describes the building orientation of the integrated component with the supporting structures, whilst Figure 4(b) shows the prototypes manufactured for the three radius values. After shoot peening, the electromagnetic performances of the components have been tested. Specifically, the scattering coefficients of the components have been measured with a HP8510c vector network analyzer calibrated between 12 GHz and 22 GHz through the technique described in Peverini et al. [23], in order to minimize cable movements and, thus, minimizing measurement errors. A number of 256 averages has been considered so as to guarantee a dynamic range of 90 dB that is necessary to carefully measure the out-of-band rejection of the components. The measured performances are compared to the predicted values in Table 2. The accordance is rather good confirming the manufacturing quality of the integrated components for all the three values of radius.

		R=50 mm	*R*=40 mm	*R*=30 mm
	Weight [g]	70	60	50
Return Loss [12.5,15] GHz	Simulated [dB]	≥ 30	≥ 25	≥ 22
	Measured [dB]	≥ 20	≥ 25	≥ 21
Rejection [17.5,21.2] GHz	Simulated [dB]	≥ 60	≥ 60	≥ 60
	Measured [dB]	≥ 60	≥ 60	≥ 60
Insertion Loss [12.5,15] GHz (ρ=12μΩcm)	Simulated [dB]	< 0.17	< 0.15	< 0.13
	Measured [dB]	< 0.2	< 0.15	< 0.16

Table 2. Comparison of the three L-PBF manufactured prototypes in term of simulated and measured performances [12].

The result of the deviation analysis between the STL model and the model produced by the L-PBF process is shown in Figure 5. The accuracy of the internal channels is confirmed by the color maps of the deviations of the scanned components from the STL model, for which the gaussian distribution has a standard deviation of approximately 0.04-0.07 mm. In particular, the internal areas have an average deviation of about 0.08 mm, 0.046 mm and 0.023 mm from the CAD model for the *R* of 50 mm, 40 mm and 30 mm, respectively. This deviation is not due to the so-called "staircase effect", typical of some additive technologies, but by the dross formation. Staircase effect is a defect that occurs during the fabrication of overhanging structures. In this study, a thin layer of 30 μm has been used for the construction of the component. The overhanging length L_o between two side-by-side layers is calculated as follows [25]:

$$L_o = \frac{t}{tan\theta} \qquad (1)$$

Where t is the layer thickness and θ is the angle of inclination between the horizontal plane and the tangent line of the surface. From Eq. (1), it can be easily inferred that the length L_o increases when the inclination angle θ decreases. This aspect can give rise to a very evident staircase effect, which negatively affects the quality of the protruding structures. For a layer thickness of 30 μm and an angle of 30° (*i.e.*, the minimum angle for self-supporting surface in AlSi10Mg alloy), the length L_o is equal to 17 μm which is less than the diameter of the melt pool (about 200 μm [26]). This value suggests that the error cannot be attributed to the staircase effect. From the stereomicroscope images of Figure 5, it can see that the deviation occurs on some edges of the overhanging areas. Overhangs necessarily involve the fusion on the powder, which has starkly different material properties than its bulk counterpart. The heat conduction rate may be hundred times smaller than bulk conduction [27], resulting in a much larger melt pool than the one obtained on an already melted layer. Because the powder particles are random packaged, inducing a variable thermal conductivity, melt pools sink deep into the powder and with recoater blade pressure and capillary forces at play, solidify into an extremely rough surface with large deformities called "dross". Formation of dross is considered the most difficult manufacturing defect to control in the L-PBF process. This defect causes both a great surface roughness and a poor geometrical precision of the overhanging surfaces. Analyzing the process parameters used, three different energy density *E* [28, 29] of 70 J/mm^3, 79 J/mm^3 and 47.79 J/mm^3 have been used for down-skin, up-skin and core, respectively. According to some studies [30,

31], the formation of a small melt pool can reduce the occurrence of the dross and also significantly improve the quality of manufacture of the down-skin surface. However, the use of a low *E* (about 48 J/mm^3) can effectively reduce the size of the melt pool, but it leads to the partial fusion of the manufactured part causing an unfavorable link between the nearby melting tracks, that is a detrimental effect for the manufacturing success of full-density L-PBF overhanging parts. If the problem is tackled based on the value of the density energy, it would be enough to remain in a range of 60 – 80 J/mm^3 [29], in order to solve the defects due to dross formation. However, the present case-study has shown that the use of an energy value of 70 J/mm^3 also leads to dross formation. The reason is that the energy value depends on the numerical combination of the process parameters (laser power, scan speed, hatching distance and layer thickness). The same value can be obtained with different process parameters leading to different results [26, 28, 32]. Surely, the formation of spatter and dross is due to the high laser absorption factor of the powder compared to the solid metal of the part. Moreover, some areas in the prototypes with R = 40 and 30 mm has required supports having angles less than 35°. Figure 6 shows the upper area of the component in which the internal part corresponds to the downward facing surfaces. The images are obtained by using Materialize's Magics software. This software is widely used in PBF processes to orient components and to insert supports. If 45° is selected as the threshold angle for the self-supporting condition, the components with R = 40 and 30 mm require supports in the surfaces and edges that are highlighted in yellow in Figure 6(b) and 6(c)). If the threshold angle is gradually reduced, it turns out that no edge is highlighted for both the components when the angle is smaller than 37°. The component with R = 50 mm already at 45° has all internal self-supporting surfaces, whilst only the edges are non-self-supporting areas. For achieving the self-supporting condition also for the edges, it would be necessary to decrease the threshold angle to 23°, but this value is much lower than the limit for AlSi10Mg alloy (30°), thus making edges inaccurate. Therefore, these areas exhibit a higher dross formation, because no supports can be used in the internal channels. The formation of dross in the edges and on the lower faces is less critical for the prototype with R = 30 mm, probably because of the smaller geometry compared to the other two prototypes. The lower surface, with that orientation, has a greater thermal conductivity with the solid part than with the powder, thus reducing the dross formation. There is also another expect that may have amplified the effect on the inaccuracy of the edges. Indeed, the edge can be considered a small feature of a model. If a feature has dimensions comparable to the hatching distance, the actual position of the contour of the model could significantly influence the creation of the hatch line. This can cause both positional and dimensional errors in the final shape [33].

The surface roughness measured on the down- and up-skin faces is about R_a of 8 μm ± 1.3 μm and R_z of 62.3 μm ± 0.34 μm for all three components, showing a certain consistency of the results obtainable with the process parameters used. In all three components, there are a certain number of particles that are not completely merged. These particles inside the channels are not easily removable with the cleaning of the samples by shot peening, especially when the channels have a non-linear geometry as in this case.

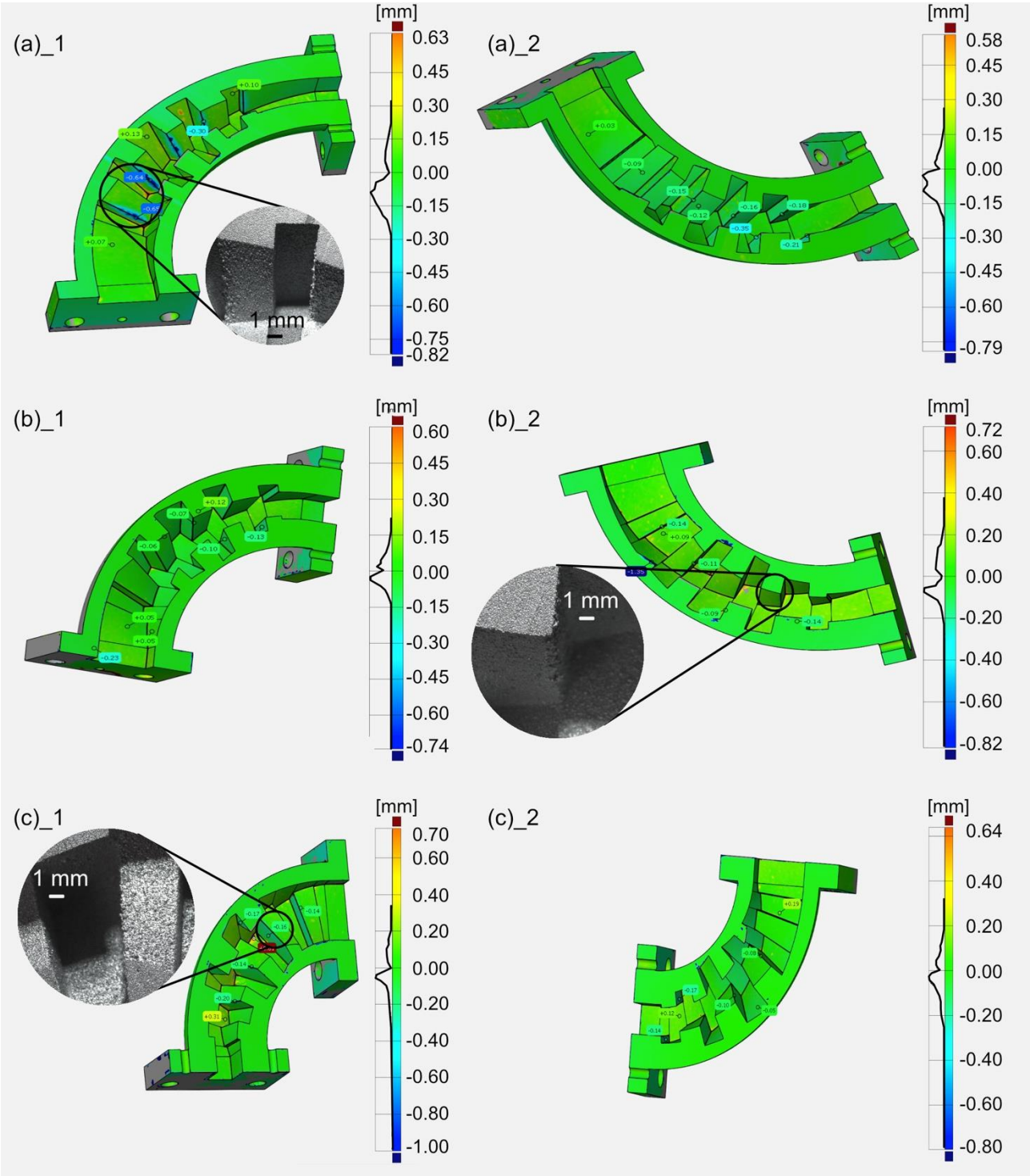

Figure 5. Deviation color maps with regard to the accuracy of the two parts of the prototypes: (a) *R* = 50 mm, (b) *R* = 40 mm, (c) *R*= 30 mm.

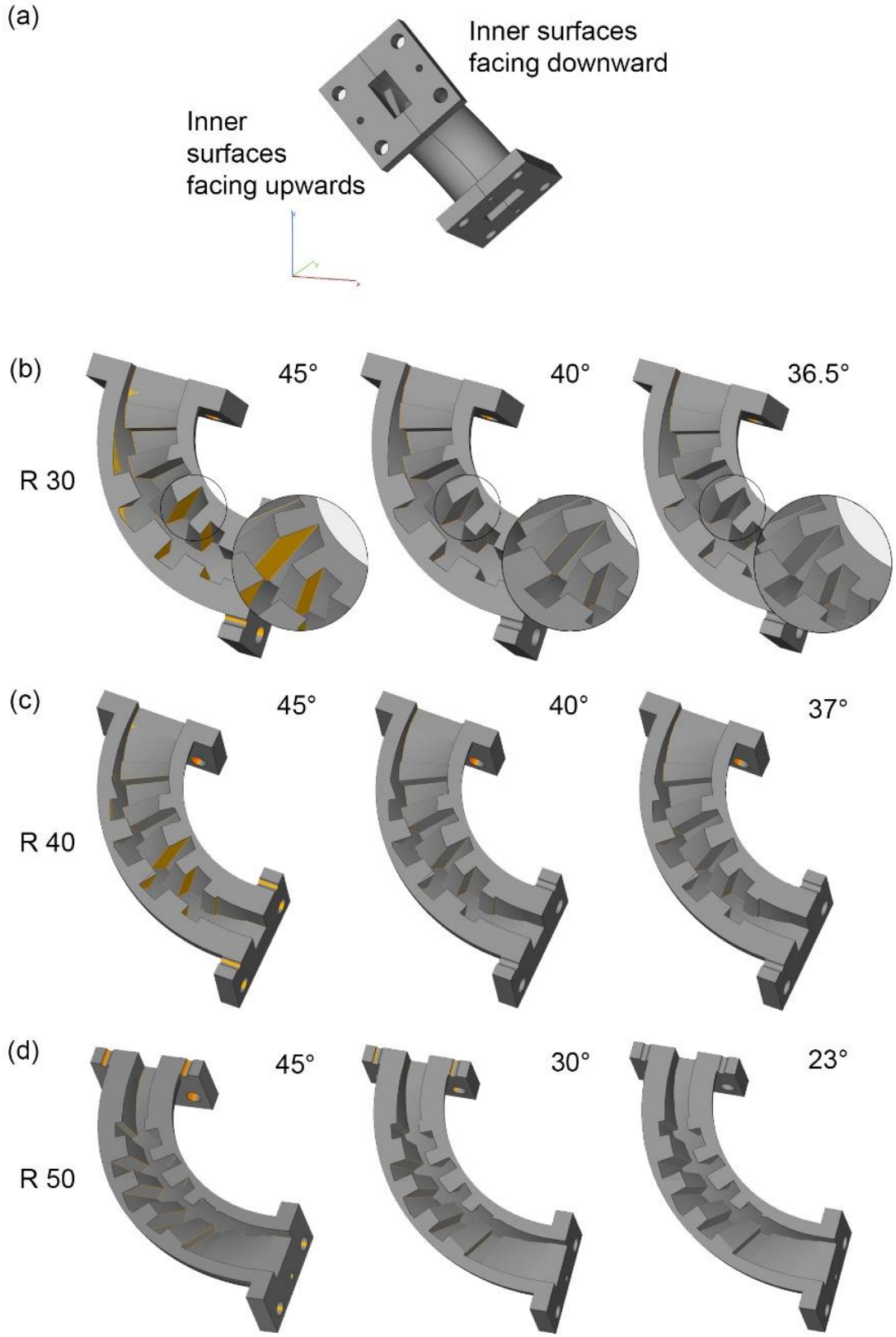

Figure 6. (a) The components were sectioned in two parts: the lower one in which the inner zone corresponds mostly to the up-skin and the upper area in which the internal part corresponds to the down-skin. Non-self-supporting areas highlighted in yellow for three different angle thresholds for the self-supporting condition: (b) R = 30 mm, (c) R = 40 mm, and (d) R = 50 mm.

4. Conclusion

The results achieved in this study in terms of dimensional accuracy of a complex radio-frequency component show the potential of the L-PBF process in the dimensional reduction of waveguide components for space and terrestrial communications.

The component with R = 30 mm has a high internal channel accuracy with a deviation about of 0.023 mm from the CAD model. This accuracy combined with the reduced surface roughness of R_a of 8 μm ± 1.3 μm makes the L-PBF process suitable for integrated production of waveguide components. However, in order to achieve this accuracy, it is necessary an accurate selection of the conversion parameters from the 3D CAD model to the STL file, of the building orientation, and of the process parameters. Generally, the recommended value for the deviation control of the STL file is $1/20^{th}$ of the layer thickness and, in any case, above 1μm. Exporting with a lower tolerance has no effect on print quality, whilst increases the size of the file that may not be manageable by the machine software. A good setting for the angle control is often 10 degrees. The orientation of the component must already be decided during the design of the component, and the process parameters have to be optimized to obtain dense and accurate components.

However, for the intended radio-frequency application, there are still inherent problems with the technology (e.g., surface roughness) that currently affects the electromagnetic performances.

References

[1] Sorrentino R, Peverini OA. Additive manufacturing: A key enabling technology for next-generation microwave and millimeter-wave systems [point of view]. Proc. IEEE 2016. https://doi.org/10.1109/JPROC.2016.2577327.

[2] Montejo-Garai JR, Saracho-Pantoja IO, Leal-Sevillano CA, Ruiz-Cruz JA, Rebollar JM. Design of microwave waveguide devices for space and ground application implemented by additive manufacturing. Proc. 2015 Int. Conf. Electromagn. Adv. Appl. ICEAA 2015, 2015. https://doi.org/10.1109/ICEAA.2015.7297128.

[3] Laplanche E, Feuray W, Sence J, Perigaud A, Tantot O, Delhote N, et al. Additive manufacturing of low cost and efficient proof of concepts for microwave passive components. IET Microwaves, Antennas Propag 2017. https://doi.org/10.1049/iet-map.2017.0157.

[4] Liu B, Gong X, Chappell WJ. Applications of layer-by-layer polymer stereolithography for three-dimensional high-frequency components. IEEE Trans. Microw. Theory Tech., 2004. https://doi.org/10.1109/TMTT.2004.837165.

[5] Le Sage GP. 3D Printed Waveguide Slot Array Antennas. IEEE Access 2016. https://doi.org/10.1109/ACCESS.2016.2544278.

[6] Booth P, Roberts R, Szymkiewicz M, Hartwanger C. Using additive manufacturing for feed chain and other passive microwave components. 2017 11th Eur. Conf. Antennas Propagation, EUCAP 2017, 2017. https://doi.org/10.23919/EuCAP.2017.7928730.

[7] Peverini OA, Addamo G, Lumia M, Virone G, Calignano F, Lorusso M, et al. Additive manufacturing of Ku/K-band waveguide filters: A comparative analysis among selective-laser melting and stereolithography. IET Microwaves, Antennas Propag 2017. https://doi.org/10.1049/iet-map.2017.0151.

[8] Van Caekenberghe K, Bleys P, Craeghs T, Pelk M, Bael S Van. A W-band waveguide fabricated using selective laser melting. Microw Opt Technol Lett 2012. https://doi.org/10.1002/mop.27121.

[9] Vandenbroucke B, Kruth JP. Selective laser melting of biocompatible metals for rapid manufacturing of medical parts. 17th Solid Free. Fabr. Symp. SFF 2006, 2006.

[10] Calignano F. Design optimization of supports for overhanging structures in aluminum and titanium alloys by selective laser melting. Mater Des 2014. https://doi.org/10.1016/j.matdes.2014.07.043.

[11] Wang D, Yang Y, Yi Z, Su X. Research on the fabricating quality optimization of the overhanging surface in SLM process. Int J Adv Manuf Technol 2013. https://doi.org/10.1007/s00170-012-4271-4.

[12] Peverini OA, Lumia M, Addamo G, Paonessa F, Virone G, Tascone R, et al. Integration of an H -Plane Bend, a Twist, and a Filter in Ku/K-Band Through Additive Manufacturing. IEEE Trans Microw Theory Tech 2018. https://doi.org/10.1109/TMTT.2018.2809505.

[13] Trevisan F, Calignano F, Lorusso M, Pakkanen J, Aversa A, Ambrosio EP, et al. On the selective laser melting (SLM) of the AlSi10Mg alloy: Process, microstructure, and mechanical properties. Materials (Basel) 2017. https://doi.org/10.3390/ma10010076.

[14] Delgado J, Ciurana J, Serenó L. Comparison of forming manufacturing processes and selective laser melting technology based on the mechanical properties of products. Virtual Phys Prototyp 2011. https://doi.org/10.1080/17452759.2011.613597.

[15] Lu Y, Wu S, Gan Y, Huang T, Yang C, Junjie L, et al. Study on the microstructure, mechanical property and residual stress of SLM Inconel-718 alloy manufactured by differing island scanning strategy. Opt Laser Technol 2015. https://doi.org/10.1016/j.optlastec.2015.07.009.

[16] Brandl E, Heckenberger U, Holzinger V, Buchbinder D. Additive manufactured AlSi10Mg samples using Selective Laser Melting (SLM): Microstructure, high cycle fatigue, and fracture behavior. Mater Des 2012. https://doi.org/10.1016/j.matdes.2011.07.067.

[17] Townsend A, Racasan R, Blunt L. Surface-specific additive manufacturing test artefacts. Surf Topogr Metrol Prop 2018. https://doi.org/10.1088/2051-672X/aabcaf.

[18] Fousová M, Vojtěch D, Doubrava K, Daniel M, Lin CF. Influence of inherent surface and internal defects on mechanical properties of additively manufactured Ti6Al4V alloy: Comparison between selective laser melting and electron beam melting. Materials (Basel) 2018. https://doi.org/10.3390/ma11040537.

[19] Triantaphyllou A, Giusca CL, Macaulay GD, Roerig F, Hoebel M, Leach RK, et al. Surface texture measurement for additive manufacturing. Surf Topogr Metrol Prop 2015. https://doi.org/10.1088/2051-672X/3/2/024002.

[20] Witkin DB, Patel DN, Helvajian H, Steffeney L, Diaz A. Surface Treatment of Powder-Bed Fusion Additive Manufactured Metals for Improved Fatigue Life. J Mater Eng Perform 2019. https://doi.org/10.1007/s11665-018-3732-9.

[21] Peverini OA, Addamo G, Virone G,Tascone R, Orta R. A Spectral-Element Method for the Analysis of 2-D Waveguide Devices With Sharp Edges and Irregular Shapes, IEEE Trans Microw Theory Tech 2011. https://doi.org/DOI: 10.1109/TMTT.2011.2144991.

[22] Calignano F. Investigation of the accuracy and roughness in the laser powder bed fusion process. Virtual Phys Prototyp 2018. https://doi.org/10.1080/17452759.2018.1426368.

[23] Peverini OA, Addamo G, Tascone R, Virone G, Orta R. Extended Through-Short-Delay Technique for the Calibration of Vector Network Analyzers with Non-mating Waveguide Ports, IEEE Trans Microw Theory Tech 2010. https://doi.org/10.1109/TMTT.2009.2038455.

[24] Ventola L, Robotti F, Dialameh M, Calignano F, Manfredi D, Chiavazzo E, et al. Rough surfaces with enhanced heat transfer for electronics cooling by direct metal laser sintering. Int J Heat Mass Transf 2014. https://doi.org/10.1016/j.ijheatmasstransfer.2014.03.037.

[25] Yadroitsev I, Thivillon L, Bertrand P, Smurov I. Strategy of manufacturing components with designed internal structure by selective laser melting of metallic powder. Appl Surf Sci 2007. https://doi.org/10.1016/j.apsusc.2007.08.046.

[26] Calignano F, Cattano G, Manfredi D. Manufacturing of thin wall structures in AlSi10Mg alloy by laser powder bed fusion through process parameters. J Mater Process Technol 2018. https://doi.org/10.1016/j.jmatprotec.2018.01.029.

[27] Wei LC, Ehrlich LE, Powell-Palm MJ, Montgomery C, Beuth J, Malen JA. Thermal conductivity of metal powders for powder bed additive manufacturing. Addit Manuf 2018. https://doi.org/10.1016/j.addma.2018.02.002.

[28] Scipioni Bertoli U, Wolfer AJ, Matthews MJ, Delplanque JPR, Schoenung JM. On the limitations of Volumetric Energy Density as a design parameter for Selective Laser Melting. Mater Des 2017. https://doi.org/10.1016/j.matdes.2016.10.037.

[29] Zhang B, Li Y, Bai Q. Defect Formation Mechanisms in Selective Laser Melting: A Review. Chinese J Mech Eng (English Ed 2017. https://doi.org/10.1007/s10033-017-0121-5.

[30] Chen H, Gu D, Xiong J, Xia M. Improving additive manufacturing processability of hard-to-process overhanging structure by selective laser melting. J Mater Process Technol 2017. https://doi.org/10.1016/j.jmatprotec.2017.06.044.

[31] Charles A, Elkaseer A, Thijs L, Hagenmeyer V, Scholz S. Effect of process parameters on the generated surface roughness of down-facing surfaces in selective laser melting. Appl Sci 2019. https://doi.org/10.3390/app9061256.

[32] Prashanth KG, Scudino S, Maity T, Das J, Eckert J. Is the energy density a reliable parameter for materials synthesis by selective laser melting? Mater Res Lett 2017. https://doi.org/10.1080/21663831.2017.1299808.

[33] Yang L, Gong H, Dilip S, Stucker B. An investigation of thin feature generation in direct metal laser sintering systems. Proc 26th Annu Int Solid Free Fabr Symp 2014.